



PAPER

## Simultaneous multi-spatial scanning optical coherence tomography (OCT) based on spectrum-slicing of a broadband source

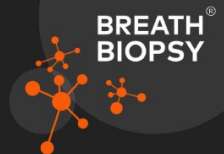
To cite this article: Taye Mekonnen *et al* 2019 *Meas. Sci. Technol.* **30** 045203

View the [article online](#) for updates and enhancements.

### You may also like

- [A review of low-cost and portable optical coherence tomography](#)  
Ge Song, Evan T Jelly, Kengyeh K Chu et al.
- [Functional optical coherence tomography: principles and progress](#)  
Jina Kim, William Brown, Jason R. Maher et al.
- [Cross-sectional imaging through scattering media by quantum-mimetic optical coherence tomography with wavefront shaping](#)  
Tomohiro Shirai and Ari T Friberg

# Breath Biopsy Conference



Join the conference to explore the **latest challenges** and advances in **breath research**, you could even **present your latest work!**



5th & 6th November  
Online



**Register now for free!**

# Simultaneous multi-spatial scanning optical coherence tomography (OCT) based on spectrum-slicing of a broadband source

Taye Mekonnen<sup>1</sup> , Agisilaos Kourmatzis<sup>2</sup>, Jason Amatoury<sup>3</sup> and Shaokoon Cheng<sup>1</sup>

<sup>1</sup> School of Engineering, Macquarie University, Sydney, Australia

<sup>2</sup> School of Aerospace, Mechanical and Mechatronic Engineering, University of Sydney, Sydney, Australia

<sup>3</sup> Biomedical Engineering Program, Maroun Semaan Faculty of Engineering and Architecture, American University of Beirut, Beirut, Lebanon

E-mail: [shaokoon.cheng@mq.edu.au](mailto:shaokoon.cheng@mq.edu.au)

Received 12 November 2018, revised 28 February 2019

Accepted for publication 4 March 2019

Published 18 March 2019



CrossMark

## Abstract

This paper reports the characterization of a novel daisy-chained multi-channel optical coherence tomography (MC-OCT) method capable of concurrent scanning at multiple sites along the sample arm length of a low coherence interferometer. For this study, a cascade of two wavelength-based beam splitters is used to split the sample arm beam into three channels, forming three imaging (sensing) units. Channel-specific free-space beam paths are introduced in the sample arm to ensure equal optical path lengths amongst the different sensing beams, and hence, a single reference reflector is employed for simultaneous interrogation of signals reflected from samples (or from different spots of a sample). Realistic simulation is carried out to study the properties of the interference patterns such as axial resolutions and spurious side-lobes. Using a broadband light source of 50 nm bandwidth at 840 nm centre wavelength, the achieved axial resolutions of 24.23  $\mu\text{m}$ , 17.81  $\mu\text{m}$  and 20.49  $\mu\text{m}$  for channels 1, 2 and 3, respectively, are in good correlation with simulations. Experimental results on a 3D-printed phantom further validate the imaging functionality of the system. The findings demonstrate a new single source and single interferometric-based MC-OCT method that can feasibly improve the transverse-scan throughput of conventional OCT.

Keywords: optical coherence tomography, interferometer, multi-channel, concurrent scanning, imaging unit, wavelength channel

(Some figures may appear in colour only in the online journal)

## 1. Introduction

Optical coherence tomography (OCT) is a widely known interferometric imaging technique which has attracted considerable attention in applications from quantifying the geometry of biological conduits such as airways and blood vessels [1–6], to use in various industrial fields such as inspection of touch-screen panels and identification of counterfeit notes [7, 8]. In all these applications conventional OCT generally consists of a low-coherence broadband light source which is

split to produce two separate beams, a sample arm and reference arm. A detection head (probe) in the sample arm directs a light beam at the sample of interest and scans the reflected light. The back-scattered light is transported towards an interferometer where it interferes with a reference beam, which is reflected from a flat optical mirror. From the resulting interference pattern, high-resolution topographical information of the reflecting sample spot (or section) can be obtained.

In practice, endoscopic OCT is generally implemented through the use of a small probe-mounted micro-optics

assembly which provides the high-resolution image. In the example of a biological lumen, a circumferential scan is achieved through a probe spinning procedure, using a torque coil or microelectromechanical (MEM) motors [9–12]. Currently, the reconstruction of full lumen geometries (such as respiratory airways and blood vessels) requires traversing the probe manually in the lumen to perform multiple circumferential scans at different lumen sites. While the overall geometry can be analysed from the averaged circumferential images, such a technique is unable to provide accurate measurements of lumen deformation, which changes dynamically and non-uniformly along the lumen length during physiological functions. In the human upper airway, for example, maintenance of pharyngeal patency at different phases of respiration is underpinned by complex mechanisms that involve the concurrent dilation and collapse of the airway at different locations along the pharynx [13, 14]. Multi-positional lumen measurements in such applications would be useful to define appropriate treatment strategies for diseases where the location and mechanism of upper airway collapse would be relevant [15, 16]. In addition, although the industrial applications of single-channel OCT devices for product quality assurance are ubiquitous, a multi-channel OCT device has the added advantage as a cost-effective solution to provide inline continuous inspection of surface profiles and subsurface structures of moving objects (product parts), for instance in the inspection of thin films during manufacturing [17]. Several studies have proposed different configurations of multi-channel OCT [18–23], however, their application is not specifically designed for applications that require the concurrent scanning of different transverse locations of a sample.

In some configurations, an extension to two channel OCT has been demonstrated through the obtainment of simultaneous en-face images of two retinal layers [24], and in other configurations, delays were introduced either exclusively to the reference arm or to both reference and sample arms for imaging at different tissue depths [25, 26]. These techniques enabled multiple coherence signals to be obtained at different tissue depths but from a single longitudinal location. Imaging at different longitudinal sites (i.e. along the sample arm length of the interferometer) has generally been limited because the optical path-length difference between the sample and reference arms should be within the coherence length of the light source.

A micro-machined fibre-optic tip design, where several fibres are arranged in a stepped linear array, can be reconfigured to enable imaging along the length of the probe and to provide cross-sectional images at different locations simultaneously [27–29]. Nevertheless, while this configuration offers multi-channel capability, it not only requires multiple interferometers but the optical arrangement of the closely-spaced fibre array at the tip of the probe may also limit its functionality in biomedical applications where significant lateral separation is required between the concurrently scanned sample sites. Similarly, the transverse spacing between adjacent imaging sites in ‘rattle plate’-based multi-beam OCT has

been limited to a fraction of 1 mm [30]. An alternative is the use of multiple light sources and spectrometers. However, this makes the overall system non-economical [31]. Considering these issues, the development of an OCT technique that is suitable for both multi-channel endoscopic applications and concurrent en-face scanning would be highly beneficial, and this forms the key aim of this study.

A new multi-channel OCT (MC-OCT) design, characterized by the simultaneous acquisition of signals using daisy-chained sensing units distributed along the length of the sample arm is presented. The experimental configuration and principle of operation of a three-channel benchtop time-domain OCT system are discussed, and results are compared with simulations to match system resolution and interference function shape. The configuration employs a cascade of dichroic filters to produce multiple wavelength channels (bands) from a single broadband optical source. Each channel, servicing a specific sensing unit, utilizes the same, single interferometer to produce interference patterns from different spots on the sample simultaneously. This is a new single source and single interferometer-based concurrent scanning technique which provides the foundation for a resource and size-optimized multi-channel OCT system while at the same time demonstrating that such a configuration is promising in the study of physiological deformation of biological lumens and in the inspection of product parts during manufacturing.

## 2. Materials and methods

### 2.1. Modelling of multi-channel OCT

Figure 1 shows the beam path diagram of a conceptual multi-channel OCT where light from a broadband source is split into reference and sensing lights, directed to reference and sample arms, respectively. The sensing light is further split into different wavelength channels, each spanning a given range of source spectra, using a cascade of high-pass dichroic filters. Thus, the channel beams hit the sample at distinct longitudinal locations.

Assuming a single-layer sample, the instantaneous electric field vectors  $E_{sn}$  and  $E_R$  reflected off the  $n$ th sample location and reference mirror, respectively, are given by (1) [32]:

$$E_{sn} = A_{sn} \exp(kd_{sn} - \omega t) \text{ and,}$$

$$E_R = A_R \exp(kd_R - \omega t) \quad (1)$$

where  $k = \frac{2\pi}{\lambda}$  is the wavenumber,  $A_{sn}$  and  $A_R$  are amplitude constants,  $d_R$  and  $d_{sn}$  are the distances from the beam splitter to the reference and the  $n$ th sample location, respectively. Therefore, the detector current,  $I$  (equation (2)), is the time average of the superposition of fields from the reference mirror and the  $N$  sample reflectors.

$$I = \left\langle \left( E_R + \sum_{n=1}^N E_{sn} \right) \cdot \left( E_R + \sum_{n=1}^N E_{sn} \right)^* \right\rangle. \quad (2)$$

Expanding equation (2) yields (3):

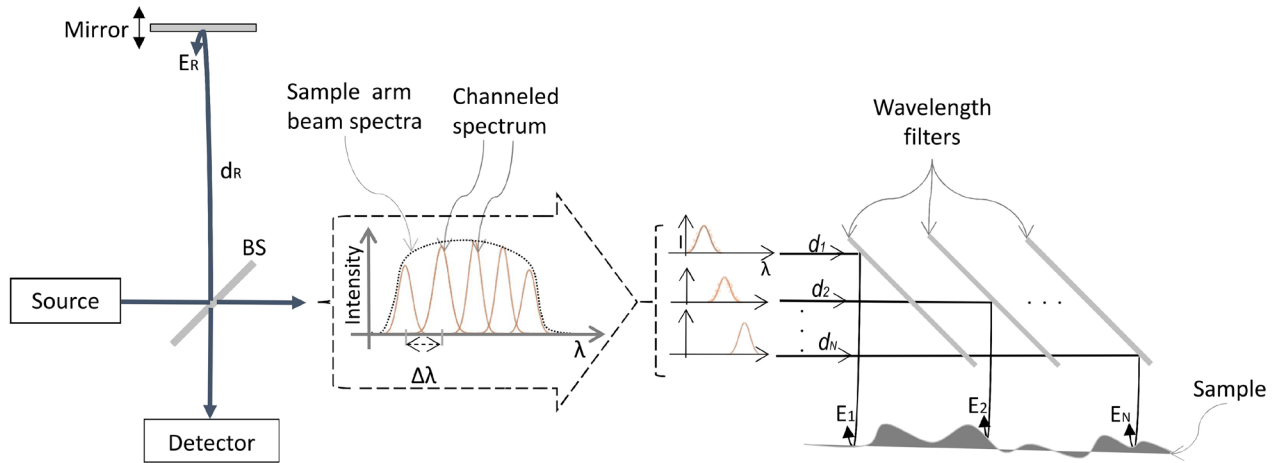


**Figure 1.** A diagram of spectrum distribution and optical paths of a simplified multi-channel OCT. BS: a 50/50 beam splitter;  $d_R$ : path-length between beam splitter and reference mirror;  $d_1, d_2, \dots, d_N$ : distance between beam splitter and sample reflectors;  $\lambda$ : wavelength;  $I$ : intensity;  $\Delta\lambda$ : difference between centre wavelengths of adjacent channels;  $E_R$  and  $E_1, E_2, \dots, E_N$  are back-scattered electric fields from reference and  $N$  sample reflectors, respectively.

$$I = \left\langle E_R^2 + \sum_{n=1}^N E_{sn}^2 + \sum_{n=1}^N (E_R \cdot E_{sn}^* + E_R^* \cdot E_{sn}) + \sum_{n=1}^N (E_{sn} \cdot E_{sm}^* + E_{sn}^* \cdot E_{sm}) \right\rangle. \quad (3)$$

The output of the interferometer (the intensity at the detector) as a function of  $k$  becomes equal to (4):

$$I(k) = \underbrace{A_R^2 + \sum_{n=1}^N A_{sn}^2}_{\text{DC terms}} + \underbrace{2A_R \sum_{n=1}^N A_{sn} \cos(2k(d_R - d_{sn}))}_{\text{Interferometric term}} + \underbrace{2 * \sum_{n \neq m=1}^N (A_{sn} A_{sm} \cos(2k(d_{sn} - d_{sm})))}_{\text{Inter-channel interference term}}. \quad (4)$$

The DC term in (4) is a path-length independent offset which is proportional to the sum of power reflectivities of the samples and the reference mirror. The interferometric (cross-correlation) term, typically referred to as the OCT interference fringe, is a function of both wavenumber and the path-length difference between the reference and sample reflectors. It results from the cross-correlation between channel beams and their corresponding range of spectra from the reference path. The inter-channel interference term represents the correlation between different sample reflectors. This term largely contributes to the DC artefact as the channel spectrums are incoherent unless there is a partial spectral overlap of adjacent channels.

A closer inspection of (4) reveals that the interferometric term yields concurrent multiple fringe bursts when the optical path-length differences,  $\Delta d = 2|d_R - d_{sn}|$ , are within the coherence length of the light source. On the other hand, the channel beams in figure 1 transverse through distinct path-lengths due to the optical geometry of the filters and location

of the reflecting sample spots. Assuming a uniform spacing,  $\Delta l$ , between adjacent filters, the minimum distance offset between the optical path-length of any two channels,  $m$  and  $n$ , can be given by equation (5):

$$2|d_{sn} - d_{sm}| = 2|n - m| \Delta l, \quad \text{where } m \neq n = 1, 2, 3, \dots, N. \quad (5)$$

As a result, single reference reflector-based multiple fringe signals can be produced from the different channels when the path-length offsets (i.e.  $|n - m| \Delta l$ ) are compensated. This can be ensured either by incorporating channel-specific delay lines in the sample/reference arm or by placing the samples at varying distances from the wavelength filters (figure 3). In an endoscopic probe, the distinct sample spots are equidistant from the axis of the probe necessitating the use of channel-specific delay lines in either arm of the interferometer. In this paper, the implementation of the second technique is discussed as a proof of concept.

## 2.2. Simulation of three-channel OCT

A simulation of three-channel OCT was carried out using multi-spatial modelling, as described in section 2.1 and using conventional virtual OCT techniques [32–34]. As discussed in section 2.1, the per channel spectra returning from samples contained a portion of source spectra as compared to the reflected reference light spectra, which was approximately identical to the light source. As a result, the interference functions of each channel were produced by cross-correlation of two spectrally differing beams. Hence, investigation of spectral mismatch effects on the interference fringe properties such as full-width-half-maximum (FWHM) resolution is essential.

The three-channel MC-OCT analysis was performed using spectral data of the SLD light source (SLD spectrum, EXALOS Inc., Switzerland) and the dichroic filters (Percent Transmission Profile, Chroma Technology Co., USA). These actual parameters were used to produce the spectral profile of the wavelength channels. The diagram in figure 2 illustrates

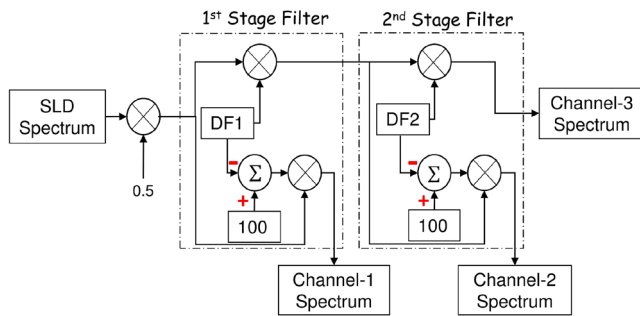


**Figure 2.** Block diagram of source spectrum splitting using a cascade of two dichroic filters to generate three wavelength channels; DF1: dichroic filter at 825 nm cut-on wavelength; and DF2: dichroic filter at 848 nm cut-on wavelength.

the optical phenomena that the sensing light beam undergoes as it travels in the sample arm of the interferometer. As it exits the beam splitter (coupler), the sensing light contains the same spectral component as the SLD source but at the half intensity level. This spectrum is decomposed into three sensing sub-spectrums by cascading two dichroic filters, DF1 and DF2. In the first stage filter, the product of the source spectrum and DF1's percent transmittance produces the transmitted spectral profile while the product of the source spectrum and percent reflection (i.e. 100—percent transmittance of DF1) produces the first wavelength channel.

A software model of the OCT system was programmed using LabVIEW, and virtual analysis was performed on each wavelength channel. The interference patterns were produced by auto-correlation of the channel spectrums as a back-scattered signal from samples and a reflected signal from the reference mirror. The characteristics of interference patterns such as axial resolution and profile of interference function in a three-channel setting were studied by comparing the simulation results with experiments.

### 2.3. Experimental setup

The schematic of the three-channel MC-OCT is shown in figure 3. This time domain configuration of the benchtop MC-OCT mainly comprised of a light source, a reference arm, sample arm (sensing unit) and a detection unit. The light source was a broadband superluminescent light emitting diode (SLD) with FWHM bandwidth of 50 nm, and a centre wavelength of 840 nm (EXS210006-01, EXALOS Inc., Switzerland), with an optical power output of 10.35 mW. The light passed through a broadband optical circulator (BPICIR-840-H7-L-08-FA, OF-LINK Communications Co., China) before it was split into sample and reference arms by a 50:50 wideband fibre-optic coupler (TW850R5A2, Thorlabs Inc., USA). Three fibre collimators (F220APC-850, Thorlabs Inc., USA) were used to collimate the out-going reference, sample and detector arm beams from this fibre-based Michelson interferometer.

The reference arm was terminated by a highly reflective mirror (BB03-E03, Thorlabs Inc., USA) mounted on a computer-controlled linear translational stage (MTS25/M-Z8, Thorlabs Inc., USA). Using this motorized stage, bundled

with a DC servo motor controller (KDC101, Thorlabs Inc., USA), the position of the reference mirror can be scanned at a maximum speed of  $2.4 \text{ mm s}^{-1}$  with an incremental resolution of  $0.05 \text{ } \mu\text{m}$ . An absorptive neutral density filter (NE20A, Thorlabs Inc., USA) was placed in the reference path to allow better fringe visibility, and therefore greater signal-to-noise ratio by attenuating the reference beam. Additionally, this filter could serve as a tool to minimize the dispersion mismatch between the reference and sample arms. However, a complete per channel dispersion compensation using this approach is limited due to the difference in the optical geometry of the reference and sample arms.

The collimated sensing beam in the sample arm was directed to a cascade of two high pass dichroic filters, with cut-on wavelengths of 825 nm and 848 nm (T825dcxrx-UF1 and T848lpxxrx, Chroma Technology Co., USA). When the sensing light hits the first filter, DF1, at an angle of  $45^\circ$ , a wavelength channel of the first sensing/imaging unit is directed sideways, perpendicular to the incoming sensing light path, while the remaining wavelength channels are transported towards the subsequent sensing units. A  $45^\circ$  line of incidence at the surface of the filters was ensured by using filter mount cages (CM1-DCH/M, Thorlabs Inc., USA). An aspheric lens (A260TM-B, Thorlabs Inc., USA) of focal length 15.29 mm was used to focus each beamlet on samples S1, S2 and S3. The samples were systematically positioned in such a way that each of the beamlets traverses approximately equal optical path lengths. In doing so, the time-of-flight delay of the reference beam was matched with reflections from the three samples. The samples were mounted on linear translation stages (PT1/M, Thorlabs Inc., USA) to enable lateral scanning (B-scan). Hence, the system acquired three A-scans in parallel using a single reference reflector.

The OCT signals were recorded with a detector unit consisting of a collimator, a similar set of dichroic filters as in the sample arm, a mirror and an array of three photodiodes (SM05PD1A, Thorlabs Inc., USA). The detected signals were amplified by custom-designed amplifier circuits, and the acquired interference pattern data was transferred to a computer system using a four-channel data acquisition device (NI-9215, National Instruments). Data was processed, and channel-specific B-scans were stitched together using custom-built LabVIEW software to construct a composite B-scan from the three channels.

Experimental studies were conducted for single- and dual-channel configurations to evaluate how the change in the number of channels affects the performance. The single-channel configuration of the schematic in figure 3 was built by removing both DF1 and DF2 filters whereas only the DF2 filter was removed during dual-channel operation. Hence, channels 2 and 3 of the three-channel setup were lumped together as a two-channel configuration. In each configuration, reflective mirrors were used to study the axial resolutions.

During some experiments, the optical path length difference between adjacent channels was adjusted to  $100 \text{ } \mu\text{m}$  to enable easier visualization of interference fringes while scanning the reference mirror position. Following initial validation with reflective samples, the imaging performance of

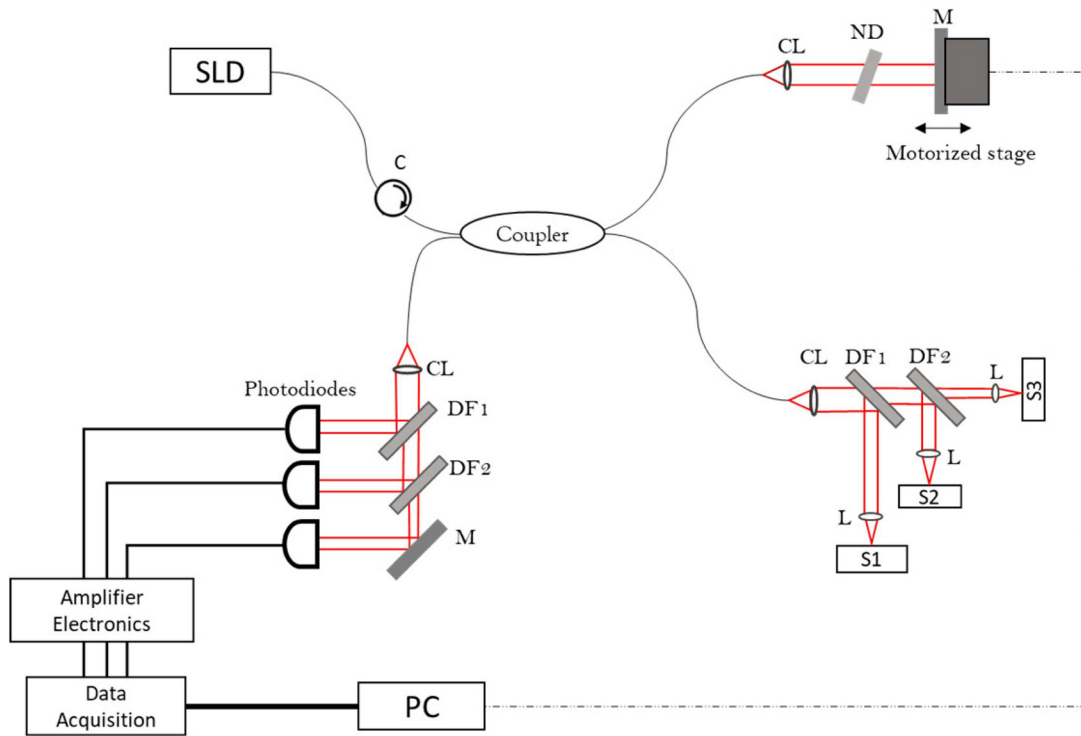


**Figure 3.** The schematic of a three-channel MC-OCT architecture. The red lines indicate free space light beam; SLD: super-luminescent diode; C: optical circulator; CL: collimator; ND: neutral density filter; M: mirror; DF1: dichroic filter at 825 nm cut-on wavelength; DF2: dichroic filter at 848 nm cut-on wavelength; L: aspheric Lens; PC: computer; S1, S2 and S3 indicate samples under channels 1, 2 and 3, respectively.

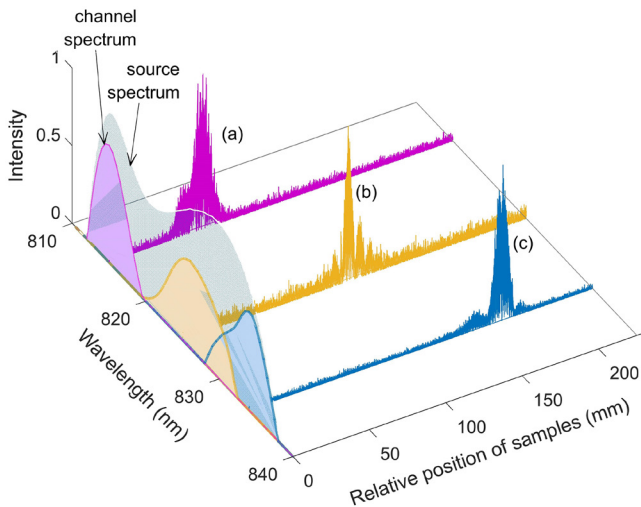


**Figure 4.** (a)–(c) Simultaneously acquired A-scan signals from channels 1, 2 and 3, respectively, of a three-channel OCT. The spectral range of each channel is indicated on the wavelength axis.

the three-channel system was validated using a 3D printed phantom with a refractive index of  $\sim 1.465$ —an optical property comparable to human soft tissue.

### 3. Results and discussion

In each of the one-, two- and three-channel configurations of the system, interference signals were obtained by changing the position of the reference reflector at a speed of 2.0 mm

**Table 1.** MC-OCT configurations and channel axial resolutions.

| Configuration  | FWHM spectrum  |                        |                                    |
|----------------|----------------|------------------------|------------------------------------|
|                | Bandwidth (nm) | Center wavelength (nm) | Axial resolution ( $\mu\text{m}$ ) |
| Single-channel | 50             | 840                    | 8.32                               |
| Two-channel    | 1st channel    | 13.5                   | 819.5                              |
|                | 2nd channel    | 36.5                   | 846                                |
| Three-channel  | 1st channel    | 13.5                   | 819.5                              |
|                | 2nd channel    | 19                     | 839                                |
|                | 3rd channel    | 17.5                   | 856.5                              |

$\text{s}^{-1}$ , corresponding to a Doppler frequency of 4.76 kHz. For this axial scanning, the interference patterns were sampled at a frequency of 95 kHz, a sampling frequency which is approximately twenty times the Doppler frequency. The fringe signals were demodulated, and the depth-resolved point spread functions (PSFs) were obtained using a digital Hilbert Transform [35].

#### 3.1. Interferograms and axial resolutions

Figure 4 shows the three depth-resolved interference fringes simultaneously collected from a single scan pass of the reference mirror position. The axial resolution of each channel was estimated from the FWHM of the depth-resolved interference fringes (PSFs). For this three-channel configuration, axial resolutions achieved were 24.23  $\mu\text{m}$ , 17.81  $\mu\text{m}$  and

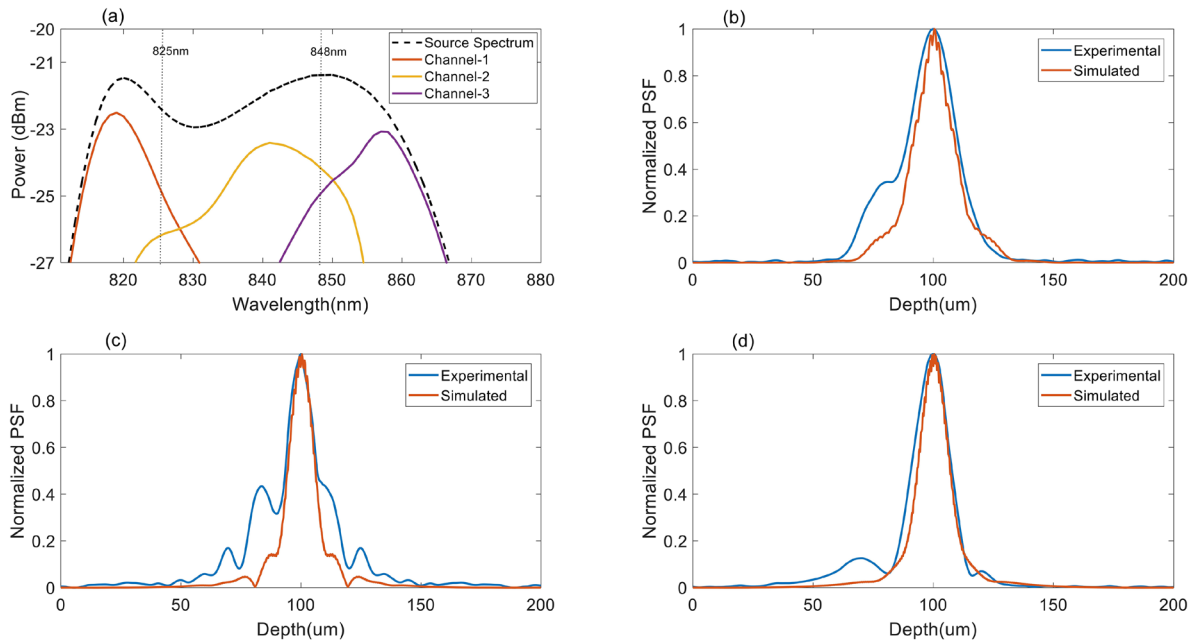


**Figure 5.** (a) Source spectrum sliced into three channels: the dotted graph indicates the spectrum of the light source while the solid lines are sub-spectrums of the three channels; (b)–(d) are comparisons of simulated and experimental PSF functions of channels 1, 2 and 3, respectively.

20.49  $\mu\text{m}$  for channels 1, 2 and 3, respectively. The variation of the resolutions is in good agreement with the FWHM channel bandwidths of 13.5 nm, 19 nm and 17.5 nm (table 1) for channels 1, 2 and 3, respectively. However, it can be noted that the numerical value of the experimental axial resolutions is slightly higher than the theoretical analysis (computed by using a coherence relation [32–34] of Gaussian channel spectra with the center wavelength and FWHM bandwidth parameters shown in table 1) which are 22.76  $\mu\text{m}$ , 16.42  $\mu\text{m}$  and 18.52  $\mu\text{m}$  for channels 1, 2 and 3, respectively. This slight broadening of the PSF is attributed to various factors such as differences in the geometry of the optics in each arm and/or the presence of the glass filters in the sample arm beam path which causes dispersion mismatch.

Side lobes appear in the channel interference functions due to the non-Gaussian profile of channel spectrums (figures 4(a)–(c)). These do not have a significant effect on the resolution as the main envelope of the interference patterns in each of the channels is at least twice the peak of the largest side-lobe. Furthermore, the first side-lobes can be suppressed by using established techniques such as pupil filters [36].

### 3.2. Simulations and experiments: a comparison of fringe patterns

Figure 5(a) depicts the three channel sub-spectrums resulting from splitting of the source spectrum, i.e. the dotted graph. The sub-spectrums were used to represent back-scattered light from the sample surfaces and the reference mirror. Hence, auto-correlation was performed by assuming identical spectra reflections from the two arms of the interferometer.

Figures 5(b)–(d) shows the comparison of the simulated PSF functions with experimental results. The axial resolution

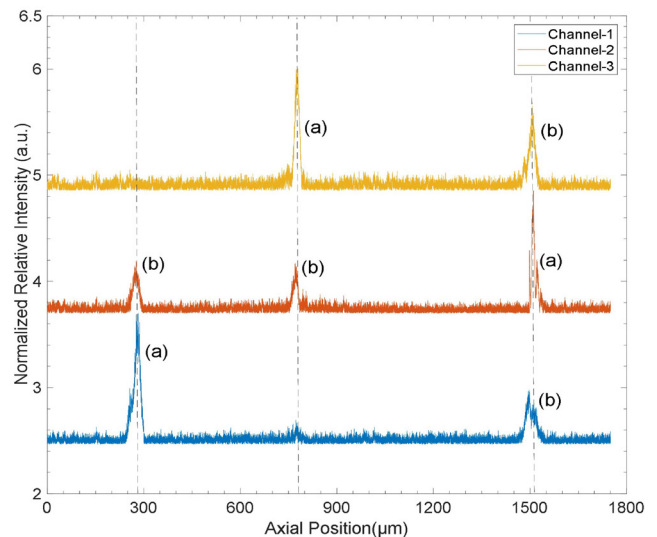


**Figure 6.** A-scans from a three-channel OCT at  $\sim 5^\circ$  alignment mismatch. (a) The actual fringe signal in a channel, (b) cross-talk/false fringes/from an adjacent channel.

from the simulated interferogram of channels 1, 2 and 3 were 18.34  $\mu\text{m}$ , 11.93  $\mu\text{m}$ , and 13.87  $\mu\text{m}$ , respectively. The PSFs of the experimental results were broader partly due to the unbalanced spectra interferometry where the wavelength interval of the back-reflected reference beam is wider than the bandwidth of each channel.

The difference in resolutions between simulations and theoretical values is attributed to the intensity distribution of the channel spectra. The transition region, the interval between reflection and transmission by the high-pass dichroic filters, spans a substantial range of wavelengths resulting in non-Gaussian channel spectra which exhibit significant tail-intensity distribution. Thus, the FWHM of the PSF is

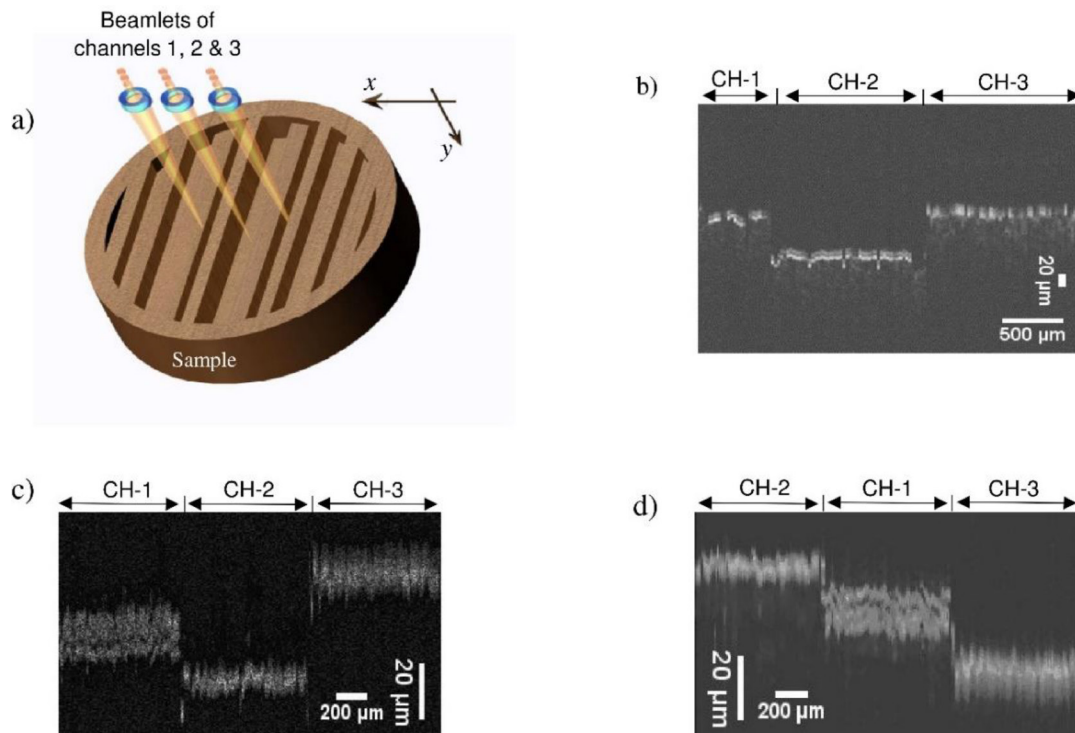


**Figure 7.** (a) Orientation of three channel incident beams on the sample, (b)–(d) representative grayscale images showing cross-sections of different grooves on the sample. CH-1, CH-2 and CH-3 depict B-scans from channels 1, 2 and 3 respectively.

reasonably small in simulations as compared to the theoretical axial resolutions obtained in section 3.1 [37].

Furthermore, the spurious side lobes from experimental results have higher peaks than simulation outputs. The dispersion mismatch and limitations in precise optical alignment are additional factors that may affect the interference pattern. Nevertheless, the similarity in the trend of the PSF function in figures 5(b)–(d) for both the experimental and simulated results clearly indicates that the wavelength channels can reproduce interferograms that can be produced by distinct light sources of equivalent bandwidths.

### 3.3. Channels of MC-OCT

The number of channels can be increased by introducing additional high pass wavelength filters. However, the maximum number of channels is limited by various factors including per channel axial resolution, the level of incident power on a sample and the spectral profile of the wavelength filters. As shown in table 1, the per channel axial resolution decreases with the increase in the number of channels for a light source with fixed bandwidth.

Expectedly, the per channel optical power incident on the sample decreases with an increase in the number of channels. The average PSF peak power drop in two- and three-channel configurations was  $-1.04$  dB and  $-2.63$  dB, respectively, relative to single-channel PSF peak power. Hence, increasing the number of channels will reduce the sample arm optical power, and this is likely to escalate due to transmission losses in the filters which will affect the sensitivity of the overall system [38].

In addition, the channel resolving limit of the detection unit results in a significant increase in the cross-talk noise with the increase in the number of channels. For the three-channel configuration, the measured average cross-talk noise power (with respect to signal peak power) was  $-5.74$  dB,  $-2$  dB, and  $-2.72$  dB for channels 1, 2 and 3, respectively.

The cross-talk was largely attributed to the alignment mismatch between the array of optical filters in the detection and imaging units that results in the redirection of fringe signals to adjacent channels. For instance, figure 6 shows the pseudo-fringes observed in adjacent channels at  $\sim 5^\circ$  alignment mismatch between the filters in the detection and imaging units. This effect can be minimized by using a high-resolution spectrometer instead of the filter-photodiode detection unit.

### 3.4. Cross-sectional (B-scans) imaging

The functionality of the three-channel configuration was further validated by using custom 3D-printed phantoms. The samples (i.e. S1, S2 and S3 in figure 3) were identical in having the geometric shape (groove pattern) similar to the item labelled 'sample' in figure 7(a). These phantoms were mounted on linear micrometer stages and translated laterally (i.e. in a perpendicular plane to the longitudinal axis of the channel beams) to obtain three B-scans simultaneously. Each sample was precisely positioned so that scanning was performed along the same line on each sample as depicted in figure 7(a), which shows the focus points (arrangement) of the beamlets when viewed from single phantom. For each B-scan, the axial location (i.e. along the y-axis) of the reflecting sample can be determined by scanning the position of the

reference mirror. The axial spatial information was used to stitch the three B-scans together and form a composite cross-sectional image.

The B-scans from each channel are represented by the segments in the grayscale images shown in figures 7(b)–(d) as each channel scans at a given step on the sample.

Figure 7(b) illustrates detection of fine-indentations on the sample as microscale ( $\sim 25$ – $100\ \mu\text{m}$ ) details are visible. The effect of channel resolutions on cross-sectional images is evident in figures 7(c)–(d). The middle segment of figure 7(c) and the left segments of figure 7(d) represent the B-scans from the highest resolution channel, i.e. channel 2. The higher the resolution of a channel, the thinner the cross-sectional segment. However, the difference between the other two segments obtained from channels 1 and 3 is hardly visible. Overall, these experimental results show the potential of a single interferometric multi-channel OCT in performing multiple spot concurrent scanning from different depths or from the same depth (en-face).

#### 4. Conclusions

In this paper, a prototype of a daisy-chained multi-channel OCT that employs a cascade of wavelength filters in the sample arm of the interferometer was presented. To the best of the authors' knowledge, the proposed design configuration is new and is the first demonstration of a technique that can potentially be tailored to a size-optimised OCT probe for applications that require multi-positional measurements. The study focused on the characterization of a three-channel configuration by scanning multiple samples (or multiple spots of different steps on a single sample). A custom 3D-printed phantom was employed as a practical test to demonstrate the capacity of the system to generate details of a sample surface.

An OCT simulation was performed using optical parameters of the SLD source and the dichroic splitters, and the feasibility of the system was demonstrated by the significant correlation between the simulation results that characterized axial resolutions and the depth-resolved interference patterns (coherence functions). The spectral mismatch between the two arms of the interferometer and the inefficiency in the dispersion compensation technique (i.e. using the ND filter) resulted in the broadening of interference PSF functions in the experiments and hence, decrease the per channel axial resolution. Channel-specific modelling of digital techniques (i.e. considering the wavelength-dependent dispersion coefficient of the filters and the sample) such as deconvolution may be applied to minimize the dispersive broadening of PSF functions. Alternatively, the system may also be modified by repeating a similar configuration of dichroic filters in the reference arm so that equal per channel optical glass paths is ensured in both arms.

The effects of change in the number of channels on the system's performance were investigated by comparing one-, two and three-channel configurations. Results from this study demonstrated that the axial resolution reduces with a higher number of channels, but this can be resolved by using a light

source with higher optical bandwidth. The image resolution obtained using the benchtop model presented in this study is well suited to study soft tissue deformations in a lumen. In the human upper airway, for example, tissue motion is typically in the range of 0.5 mm to 3 mm. Other optical properties such as the potential wavelength overlap in the adjacent channels and optical alignment mismatch between sensing and detection units could also limit the number of channels of the time domain MC-OCT system and this could be optimized by upgrading the system to a Fourier Domain-OCT technique which will provide higher spectral resolution, thereby improving the speed of data acquisition.

#### ORCID iDs

Taye Mekonnen  <https://orcid.org/0000-0003-3799-6553>

#### References

- [1] Gora M J, Suter M J, Tearney G J and Li X 2017 Endoscopic optical coherence tomography: technologies and clinical applications *Biomed. Opt. Express* **8** 2405–44
- [2] Kobayashi K, Izatt J A, Kulkarni M D, Willis J and Sivak M V Jr 1998 High-resolution cross-sectional imaging of the gastrointestinal tract using optical coherence tomography: preliminary results *Gastrointest. Endosc.* **47** 515–23
- [3] Bouma B E, Tearney G J, Compton C C and Nishioka N S 2000 High-resolution imaging of the human esophagus and stomach *in vivo* using optical coherence tomography *Gastrointest. Endosc.* **51** 467–74
- [4] Li X, Boppart S, Van Dam J, Mashimo H, Mutinga M, Drexler W, Klein M, Pitris C, Krinsky M and Brezinski M 2000 Optical coherence tomography: advanced technology for the endoscopic imaging of Barrett's esophagus *Endoscopy* **32** 921–30
- [5] Yaqoob Z, Wu J, McDowell E J, Heng X and Yang C 2006 Methods and application areas of endoscopic optical coherence tomography *J. Biomed. Opt.* **11** 063001
- [6] Sharma U and Kang J U 2007 Common-path optical coherence tomography with side-viewing bare fibre probe for endoscopic optical coherence tomography *Rev. Sci. Instrum.* **78** 113102
- [7] Choi W-J, Min G-H, Lee B-H, Eom J-H and Kim J-W 2010 Counterfeit detection using characterization of safety feature on banknote with full-field optical coherence tomography *J. Opt. Soc. Korea* **14** 316–20
- [8] Kim S-H, Kim J-H and Kang S-W 2011 Nondestructive defect inspection for LCDs using optical coherence tomography *Displays* **32** 325–9
- [9] Xu Y, Singh J, Jason T H S, Ramakrishna K, Premchandran C, Kelvin C W S, Kuan C T, Chen N, Olivo M C and Sheppard C J 2007 MEMS based non-rotatory circumferential scanning optical probe for endoscopic optical coherence tomography *Proc. of the European Conf. on Biomedical Optics* pp 6627–33
- [10] Roy S K 2015 A survey mems micromotor assemblies and applications *Int. J. Eng. Res. Gen. Sci.* **3** 59–62
- [11] Fernandez J M, Flueckiger M and Perriard Y 2008 Study of a hollow ultrasonic rotary motor *Proc. of the 2008 IEEE Int. Ultrasonics Symp.* pp 1449–52
- [12] Chen T, Zhang N, Huo T, Wang C, Zheng J-G, Zhou T and Xue P 2013 Tiny endoscopic optical coherence tomography probe driven by a miniaturized hollow ultrasonic motor *J. Biomed. Opt.* **18** 086011

- [13] Cheng S, Butler J, Gandevia S and Bilston L 2008 Movement of the tongue during normal breathing in awake healthy humans *J. Physiol.* **586** 4283–94
- [14] Cheng S, Brown E C, Hatt A, Butler J E, Gandevia S C and Bilston L E 2014 Healthy humans with a narrow upper airway maintain patency during quiet breathing by dilating the airway during inspiration *J. Physiol.* **592** 4763–74
- [15] Noble P B, West A R, McLaughlin R A, Armstrong J J, Becker S, McFawn P K, Williamson J P, Eastwood P R, Hillman D R and Sampson D D 2009 Airway narrowing assessed by anatomical optical coherence tomography *in vitro*: dynamic airway wall morphology and function *J. Appl. Physiol.* **108** 401–11
- [16] Armstrong J J, Leigh M S, Sampson D D, Walsh J H, Hillman D R and Eastwood P R 2006 Quantitative upper airway imaging with anatomic optical coherence tomography *Am. J. Respir. Crit. Care Med.* **173** 226–33
- [17] Shirazi M F, Park K, Wijesinghe R E, Jeong H, Han S, Kim P, Jeon M and Kim J 2016 Fast industrial inspection of optical thin film using optical coherence tomography *Sensors* **16** 1598
- [18] Leung M K, Mariampillai A, Standish B A, Lee K K, Munce N R, Vitkin I A and Yang V X 2009 High-power wavelength-swept laser in Littman telescope-less polygon filter and dual-amplifier configuration for multichannel optical coherence tomography *Opt. Lett.* **34** 2814–6
- [19] Jonathan E 2005 Dual reference arm low-coherence interferometer-based reflectometer for optical coherence tomography (OCT) application *Opt. Commun.* **252** 202–11
- [20] Zhou C, Wang J and Jiao S 2009 Dual channel dual focus optical coherence tomography for imaging accommodation of the eye *Opt. Express* **25** 8947–55
- [21] Baumgartner A, Hitzberger C K, Ergun E, Stur M, Sattmann H, Drexler W and Fercher A F 2000 Resolution-improved dual-beam and standard optical coherence tomography: a comparison *Graefes Arch. Clin. Exp. Ophthalmol.* **238** 385–92
- [22] Wahrlich C, Alawi S A, Batz S, Fluhr J W, Lademann J and Ulrich M 2015 Assessment of a scoring system for basal cell carcinoma with multi-beam optical coherence tomography *J. Eur. Acad. Dermatol. Venereol.* **29** 1562–9
- [23] Elyas E et al 2017 Multi-channel optical coherence elastography using relative and absolute shear-wave time of flight *PLoS One* **12** e0169664
- [24] Podoleanu A G, Dobre G M, Webb D J and Jackson D A 1997 Simultaneous en-face imaging of two layers in the human retina by low-coherence reflectometry *Opt. Lett.* **22** 1039–41
- [25] Podoleanu A G, Rogers J A, Cucu R C, Jackson D A, Wacogne B, Porte H and Gharbi T 2001 Simultaneous low coherence interferometry imaging at two depths using an integrated optic modulator *Opt. Commun.* **191** 21–30
- [26] Podoleanu A G, Cucu R G, Pedro J, Weitz R, Jackson D A and Rosen R B 2005 Hybrid configuration for simultaneous en-face OCT imaging at different depths *Proc. SPIE* **5634** 160–6
- [27] Yang V X, Munce N, Pekar J, Gordon M L, Lo S, Marcon N E, Wilson B C and Vitkin I A 2004 Micromachined array tip for multifocus fiber-based optical coherence tomography *Opt. Lett.* **29** 1754–6
- [28] Standish B A, Lee K K, Mariampillai A, Munce N R, Leung M K, Yang V X and Vitkin I A 2010 *In vivo* endoscopic multi-beam optical coherence tomography *Phys. Med. Biol.* **55** 615–22
- [29] Chen C, Cheng K H, Jakubovic R, Jivraj J, Ramjst J, Deorajh R, Gao W and Yang V X 2017 Multi-beam optical coherence tomography for microvascular imaging of human skin *in vivo Proc. SPIE* **10070** 1007017
- [30] Holmes J, Hattersley S, Stone N, Bazant-Hegemark F and Barr H 2008 Multi-channel Fourier domain OCT system with superior lateral resolution for biomedical applications *Proc. SPIE* **6847** 684700
- [31] Wartak A, Haindl R, Beer F, Augustin M, Salas M, Laslandes M, Baumann B, Pircher M and Hitzberger C K 2017 Multi-channel OCT enabling multi-directional *in vivo* imaging in the human retina *Proc. of the Bio-Optics: Design and Application* p BoM3A-3
- [32] Rao Y, Sarwade N and Makkar R 2015 Modeling and simulation of optical coherence tomography on virtual OCT *Procedia Comput. Sci.* **45** 644–50
- [33] Liu N, Dai C, Tang Y and Xi P 2014 Virtual-OCT: a simulated optical coherence tomography instrument *J. Innov. Opt. Health Sci.* **7** 1450030
- [34] Kirillin M, Meglinski I, Kuzmin V, Sergeeva E and Myllylä R 2010 Simulation of optical coherence tomography images by Monte Carlo modeling based on polarization vector approach *Opt. Express* **18** 21714–24
- [35] Liu P, Groves R M and Benedictus R 2013 Signal processing in optical coherence tomography for aerospace material characterization *Opt. Eng.* **52** 033201
- [36] Yu X, Liu X, Gu J, Cui D, Wu J and Liu L 2014 Depth extension and sidelobe suppression in optical coherence tomography using pupil filters *Opt. Express* **22** 26956–66
- [37] Hsu I J, Sun C W, Lu C W, Yang C C, Chiang C P and Lin C W 2003 Resolution improvement with dispersion manipulation and a retrieval algorithm in optical coherence tomography *Appl. Opt.* **42** 227–34
- [38] Hu Z and Rollins A M 2006 Theory of two beam interference with arbitrary spectra *Opt. Express* **14** 12751–9